Quantum and classical spins on the spatially distorted kagomé lattice: Applications to volborthite $Cu_3V_2O_7(OH)_2 \cdot 2H_2O$

Fa Wang,[1,2] Ashvin Vishwanath,[1,2] and Yong Baek Kim[3,4]
[1]*Material Sciences Division, Lawrence Berkeley Laboratories, Berkeley, California 94720, USA*
[2]*Department of Physics, University of California, Berkeley, California 94720, USA*
[3]*Department of Physics, University of Toronto, Toronto, Ontario, Canada M5S 1A7*
[4]*Kavli Institute for Theoretical Physics, University of California, Santa Barbara, California 93106, USA*
(Received 13 April 2007; revised manuscript received 3 July 2007; published 28 September 2007)

In volborthite, spin-1/2 moments form a distorted kagomé lattice of corner sharing isosceles triangles with exchange constants J on two bonds and J' on the third bond. We study the properties of such spin systems and show that despite the distortion, the lattice retains a great deal of frustration. Although subextensive, the classical ground state degeneracy remains very large, growing exponentially with the system perimeter. We consider degeneracy lifting by thermal and quantum fluctuations. To linear (spin wave) order, the degeneracy is found to stay intact. Two complementary approaches are therefore introduced, appropriate to low and high temperatures, which point to the same ordered pattern for $J' > J$. In the low-temperature limit, an effective chirality Hamiltonian is derived from nonlinear spin waves, which predicts a transition on increasing J'/J from $\sqrt{3} \times \sqrt{3}$-type order to a ferrimagnetic *chirality stripe* order with a doubled unit cell. This is confirmed by a large-n approximation on the O(n) model on this lattice. While the saddle point solution produces a line degeneracy, O($1/n$) corrections select the nontrivial wave vector of the striped chirality state. The quantum limit of spin 1/2 on this lattice is studied via exact small system diagonalization and compares well with experimental results at intermediate temperatures. We suggest that the very-low-temperature spin frozen state seen in NMR experiments may be related to the disconnected nature of classical ground states on this lattice, which leads to a prediction for NMR line shapes.

DOI: 10.1103/PhysRevB.76.094421 PACS number(s): 75.10.Hk, 75.10.−b, 75.10.Jm

I. INTRODUCTION

The study of frustrated magnetic insulators has witnessed a resurgence in recent times, with the discovery of a number of interesting materials with frustrated spin interactions. Amongst the most geometrically frustrated lattices are the pyrochlore and the kagomé lattice, and perhaps the most interesting class of systems are those that combine strong quantum fluctuations with frustration. Recently, spin-1/2 systems on the kagomé lattice have been identified, the mineral volborthite $Cu_3V_2O_7(OH)_2 \cdot 2H_2O$ (Ref. 1) and herbertsmithite.[2] In the former, the equilateral kagomé triangles are distorted into isosceles triangles, rendering two of the nearest-neighbor exchange constants different from the third. In the latter case, the kagomé lattice is believed to be structurally perfect, but with perhaps a small percentage of impurity spins. Nevertheless, both systems display low-temperature physics very different from their unfrustrated counterparts and do not show signs of ordering down to temperatures well below the exchange coupling strength.

While a lot of theoretical effort has gone into characterizing the ideal frustrated lattices, distortions of the ideal structure, although common, have received less attention.[3] In many frustrated magnets, lattice distortions occur spontaneously to relieve the frustration, leading to a strong coupling between magnetic and structural order parameters. Such "multiferroic" couplings are highly prized from the technological viewpoint for convenient manipulation of magnetism,[4] and certain frustrated magnets are natural candidates.[5] This provides further motivation for studying the effect of distortions. From the theoretical viewpoint, the partial lifting of degeneracy from distortions can lead to a more tractable level of frustration and allow for new theoretical approaches. Here, we consider the effect of lattice distortion on the kagomé lattice. The class of lattice distortions we focus on is motivated by the material volborthite, whose structure consists of corner sharing isosceles triangles. Bonds along two directions then have exchange constant J, while the bond along the third direction has exchange constant $J' = \alpha J$. In volborthite, it is not definitively known if $\alpha > 1$ or $\alpha < 1$, although a comparison of bond lengths seems to favor the former.[6] Hence, we treat both kinds of anisotropy in this paper with slightly more emphasis on the $\alpha > 1$ case.

We attack this problem first from the classical zero temperature limit. We show that for a wide range of distortions, the large classical degeneracy of the Heisenberg model on the isotropic kagomé lattice is partially lifted, and the number of coplanar ground states now scales in a subextensive fashion as the exponential of the linear system size. An interesting comparison here is with the isotropic kagomé and pyrochlore lattices, where the extensively degenerate ground state can be specified in terms of local constraints reminiscent of the Gauss's law of a lattice gauge theory.[7,8] In fact, that analogy has been carried further to describe new quantum phases of frustrated magnets corresponding to the Coulomb phase of the lattice gauge theory.[9,10] In contrast, the subextensive classical degeneracy of the distorted kagomé lattice is naturally thought of as arising from constrains on one-dimensional structures, and the "soft-spin" dispersion on this lattice features a line degeneracy in the Brillouin zone, unlike the flatband of the kagomé lattice. Both these features are shared by pure ring exchange models on the square lat-

 ©2007 The American Physical Society

tice as studied in Ref. 11, where a new spin liquid phase, the excitonic Bose liquid, was discussed.

In contrast to the isotropic kagomé system, the ground states of the distorted kagomé lattice are not connected by local moves, requiring moving an infinite number of spins to make transitions from one configuration to another. We suggest that this difference may be related to the experimental observation of spin freezing seen in NMR experiments at low temperatures in volborthite (but not in the isotropic kagomé compound herbertsmithite). The classical ground state ensemble may then be expected to capture aspects of this glassy state, which we use to make experimental predictions.

Next, we consider the following question: If a spin system on this lattice develops long-range magnetic order, what is the preferred spin pattern? The degeneracy is expected to be broken by fluctuation effects, and hence, we analyze the effect of quantum and thermally excited spin waves in the harmonic approximation. Remarkably, the spin waves are found to have a precisely flat dispersion, as in the ideal kagomé case, and do not distinguish between the classical ground states at this level. To proceed, we consider thermal fluctuations in the classical model with $\alpha > 1$ in two complementary ways, approaching from high and low temperatures. These are found to be consistent with one another and point to a new ferrimagnetic state, characterized by alternating chirality stripes, and a doubled unit cell, which we call the *chirality stripe state*. The first calculation consists of combining the low-temperature nonlinear spin-wave expansion with the effective chirality Hamiltonian technique pioneered by Henley and Chan.[12] While at the isotropic point our method picks out the $\sqrt{3}\times\sqrt{3}$ state, consistent with many other studies,[12–16] turning up the spatial anisotropy leads to a transition into a new state—the chirality stripe state. To attack the problem from the opposite, disordered limit, we consider generalization to the classical O(n) model, which is tractable in the limit $n\to\infty$ and captures the fluctuating nature of the spins at high temperatures. At the saddle point level, the flatband degeneracy of the ideal kagomé case is shrunk down to a line degeneracy for $\alpha > 1$. Fully lifting the degeneracy requires going to the next order in $1/n$, which we accomplish by utilizing the high-temperature expansion. The selected state has the same nontrivial wave vector as the chirality stripe state providing additional confirmation. In contrast, when $\alpha < 1$, the large-n saddle point itself picks out the $q=0$ wave vector.

Finally, we study the problem in the quantum limit via exact diagonalization studies on small (12-site) systems with spin-1/2. Bulk properties such as specific heat and magnetic susceptibility at intermediate to high temperatures are found to be rather insensitive to the anisotropy, and differences arise only below temperatures of about $J/5$, as seen in experiments.[1] On the other hand, the ground state of the small cluster is found to be a spin singlet and the spin gap decreases on increasing anisotropy.

The structure of this paper is as follows. In Sec. II, we discuss the classical ground states of the distorted kagomé model as well as the properties of the ground state ensemble, and possible connections to the NMR experiments on the low-temperature state in volborthite. Next, we address the question of which spin-ordered pattern is favored by fluctuations on this lattice using two approaches, first by deriving an effective chirality Hamiltonian from nonlinear spin waves in Sec. III and next via a classical large-n O(n) approach, in Sec. IV, which produce consistent results. Finally, the problem is treated in the extreme quantum limit via exact diagonalization of small systems in Sec. V. Details of calculations are relegated to three appendixes.

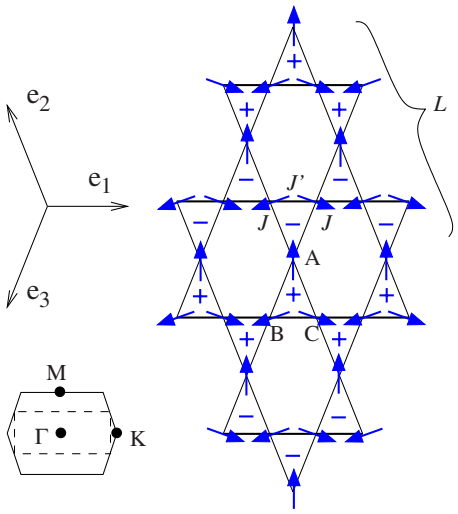

FIG. 1. (Color online) An $L\times L$ ($L=2$) distorted kagomé lattice. $\mathbf{e}_1$, $\mathbf{e}_2$, and $\mathbf{e}_3$ are three lattice translation vectors. The exchange constants J for bonds along the $\mathbf{e}_2$ and $\mathbf{e}_3$ directions are equal, but different from $J'=\alpha J$, the exchange constant for bonds along the $\mathbf{e}_1$ direction. For volborthite, it is believed that $\alpha > 1$. Γ, M, and K are high symmetry points in the Brillouin zone (BZ). The proposed spin-ordered state has alternating positive and negative chirality stripes and Fourier components at Γ and M points in BZ. Dashed rectangle is the reduced BZ for the doubled magnetic unit cell.

II. CLASSICAL GROUND STATES

Consider the antiferromagnetic Heisenberg model on the distorted kagomé lattice (Fig. 1) with different couplings for bonds on the three principal directions,

$$H = \sum_{\text{triangles}} (J_{AB}\mathbf{S}_A\cdot\mathbf{S}_B + J_{BC}\mathbf{S}_B\cdot\mathbf{S}_C + J_{CA}\mathbf{S}_C\cdot\mathbf{S}_A)$$
$$= \frac{\prod J}{2}\sum_{\text{triangles}}\left(\frac{\mathbf{S}_A}{J_{BC}} + \frac{\mathbf{S}_B}{J_{CA}} + \frac{\mathbf{S}_C}{J_{AB}}\right)^2 - \text{constant},$$

where $\mathbf{S}$ are quantum or classical spins, ΠJ means $J_{AB}J_{BC}J_{CA}$, and A, B, and C are indices for the three sublattices.

If J_{AB}, J_{BC}, and J_{CA} are all different, we call the lattice *fully distorted kagomé lattice*. In this paper, however, we consider mainly the *distorted kagomé lattice* in which $J_{AB}=J_{CA}\neq J_{BC}$. For simplicity, we set $J_{AB}=J_{CA}=1$ and $J_{BC}=\alpha$. The Hamiltonian simplifies to the following form:

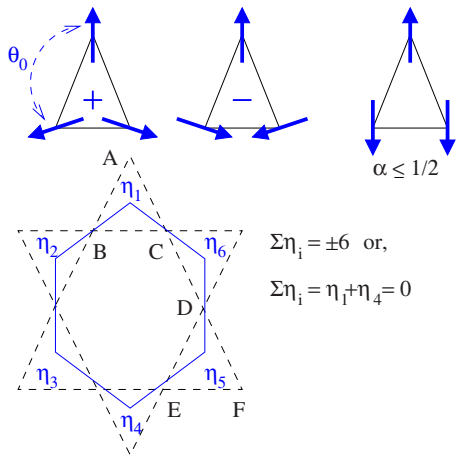

FIG. 2. (Color online) Ground states of a single triangle [$\theta_0 = \arccos(-1/2\alpha)$], definition of chirality variables, and constraint on the six chirality variables for the distorted kagomé model on a single hexagon of the honeycomb chirality lattice. *ABCDEF* are labels of six spin sites used to calculate the effective chirality interactions in a later section.

$$H = \sum_{\text{triangles}} (\mathbf{S}_A \cdot \mathbf{S}_B + \alpha \mathbf{S}_B \cdot \mathbf{S}_C + \mathbf{S}_C \cdot \mathbf{S}_A)$$
$$= \frac{\alpha}{2} \sum_{\text{triangles}} \left[\left(\frac{1}{\alpha} \right) \mathbf{S}_A + \mathbf{S}_B + \mathbf{S}_C \right]^2 - \text{constant}. \quad (1)$$

There are two simple limits. In one limiting case, $\alpha \to 0$, the lattice becomes a decorated square lattice, with additional sites at the midpoints of square lattice edges. In the other, quasi-one-dimensional (quasi-1D), limit $\alpha \to \infty$, the lattice turns into decoupled antiferromagnetic chains and "free" spins.

From the lattice structure,[6] especially the Cu-O bond lengths data of volborthite, we expect that $\alpha > 1$ in that material, although there are no direct experimental data available or quantitative first principles calculations available yet. Hence, the $\alpha < 1$ case is also considered in some of the following theoretical treatments.

The first step of studying the classical ground states on the lattice is to solve the classical ground states of a single triangle. Setting the "cluster spin" in Eq. (1) to zero, we can solve the angle between *A*-site spin and *B*(*C*)-site spin, denoted as $\theta_0 = \arccos(-1/2\alpha)$ (see Fig. 2). Since $\alpha \neq 1$, this angle will be, in general, incommensurate to 2π. We ignore the accidental commensurate cases in the following discussion since they form a measure-zero set of α. Then, the (three-state) Potts model description for the coplanar ground states of the isotropic kagomé case does not work for the distorted kagomé lattice.

A special case is $\alpha < 1/2$. In this case, there is no way that the cluster spin can be zero and the classical ground state is a collinear state with *A*-site spin antiparallel to *B*(*C*)-site spin (Fig. 2). Thus, for $\alpha \leqslant 1/2$, the classical ground state is collinear and there is no degeneracy except a global spin rotation. Notice that the lattice becomes bipartite (not frustrated) in the limit $\alpha = 0$. This classical consideration shows that the frustration of *BC* bonds is ineffective for nonzero $\alpha \leqslant 1/2$. Later, we will see from exact diagonalization study that this naive classical picture survives in quantum regime. The classical collinear state has a macroscopic net moment and is a "ferrimagnetic" state.

For $\alpha > 1/2$ case, we expect that coplanar classical ground states are favored by thermal or quantum fluctuations, and there will be zero-energy band(s) for the O(n) model with $n \geqslant 3$, because the Hamiltonian in Eq. (1) can be written as a sum of squares of cluster spins.[17] Then, it is convenient to utilize the chirality variables used in the isotropic kagomé model.[14] The chirality variables are Ising variables living at the centers of triangles, thus forming a honeycomb lattice. The positive or negative chirality variable represents the cluster of three spins on a triangle rotating counterclockwise or clockwise when one goes from *A* to *B* and then to *C* site, or $\mathbf{S}_A \times (\mathbf{S}_B - \mathbf{S}_C)$ pointing toward the $+z$ or $-z$ direction, assuming all spins lie in the x-y plane (Fig. 2).

It should be emphasized that the chirality variables are *not* independent. They determine how spin rotates (counterclockwise or clockwise) when one walks along a bond, but after walking along a closed loop on the lattice, the spin should go back to the initial direction. We need only to consider length-six hexagonal loops on the (distorted) kagomé lattice. Each one of these loops will impose a constraint on the six chirality variables η in the corresponding hexagon in the honeycomb chirality lattice (Fig. 2),

$$\eta_1(2\theta_0) - \eta_2\theta_0 - \eta_3\theta_0 + \eta_4(2\theta_0) - \eta_5\theta_0 - \eta_6\theta_0 = 0, \quad \text{mod } 2\pi. \quad (2)$$

For the isotropic kagomé antiferromagnet, $\theta_0 = 2\pi/3$, and the constraint simplifies to $\Sigma_{i=1}^6 \eta_i = \pm 6$ or 0. There are 22 allowed patterns on a single hexagon out of $2^6 = 64$ combinations. For the distorted kagomé model, θ_0 is incommensurate to 2π and the constraint is more restrictive: $\Sigma_{i=1}^6 \eta_i = \pm 6$ or $\Sigma_{i=1}^6 \eta_i = 0$ and $\eta_1 + \eta_4 = 0$. The last equation is the new constraint compared to the isotropic kagomé lattice. Note that this constraint holds for all $\alpha \neq 1$, as long as a coplanar (noncollinear) ground state is favored, i.e., $\alpha > 1/2$. There are only 14 allowed patterns on a single hexagon. For the fully distorted kagomé lattice, the constraint is even more restrictive: $\Sigma_{i=1}^6 \eta_i = \pm 6$ or $\eta_1 + \eta_4 = \eta_2 + \eta_5 = \eta_3 + \eta_6 = 0$. There are only ten allowed patterns on a single hexagon.

A. Properties of coplanar ground states on distorted kagomé lattice

The degree of degeneracy for these models on a lattice is a much more subtle problem. From Baxter's solution,[18] we know that the degeneracy of the coplanar ground states of the isotropic kagomé antiferromagnet (or three-state Potts antiferromagnet) is extensive, $\exp(0.379N)$, where N is the number of kagomé unit cells.

By counting the allowed chirality patterns for the distorted kagomé model with the $L \times L$ open boundary geometry in Fig. 1 up to $L = 9$, we conclude that the degeneracy is "sub-extensive," about $\exp(2.2L)$. Table I lists the exact enumeration result.

TABLE I. Exact enumeration results for $L\times L$ open boundary chirality lattice in the geometry of Fig. 1. The number of classical ground states N_{GS} for isotropic and for distorted kagomé lattices are shown. The tendency to order in different patterns [$q=0(\Gamma)$, $\sqrt{3}\times\sqrt{3}(K)$, and stripe ($M$) patterns] is compared by evaluating mean-square values of relevant chirality combinations [$\langle m_\Gamma^2\rangle$, $\langle m_K^2\rangle$, and $\langle m_M^2\rangle$ respectively].

	Kagomé			Distorted		
L	N_{GS}	$\frac{\langle m_\Gamma^2\rangle}{\langle m_K^2\rangle}$	$\frac{\langle m_M^2\rangle}{\langle m_K^2\rangle}$	N_{GS}	$\frac{\langle m_\Gamma^2\rangle}{\langle m_K^2\rangle}$	$\frac{\langle m_M^2\rangle}{\langle m_K^2\rangle}$
1	22	0.50	1.00	14	0.64	1.00
2	952	0.32	0.90	168	0.62	1.03
3	84048	0.22	0.92	1864	0.61	1.25
4	15409216	0.17	0.84	19724	0.61	1.25
5				201584	0.61	1.31
6				2008276	0.61	1.35
7				19596536	0.61	1.45
8				188078644	0.60	1.41
9				1779795056	0.60	1.48

Appendix A derives the asymptotic formula of the degeneracy by transfer matrix method for a slightly different geometry with periodic boundary condition. The subextensive behavior is proven by rigorous upper and lower bounds and the asymptotic formula.

For fully distorted kagomé model, the degeneracy is also subextensive, about $\exp(1.4L)$ for the geometry in Fig. 1.

One should be aware that the constant in the exponent depends on geometry and boundary conditions. Notice that Appendix A uses another geometry so that the result is not exactly the same as the enumeration results, although they both show subextensive behavior.

Another issue about classical degeneracy is the existence of the so-called weather-vane modes. In the isotropic kagomé model, those local zero-energy modes were argued to favor the $\sqrt{3}\times\sqrt{3}$ state.[14] However, one can easily prove that in the distorted kagomé O(3) model, there is no *local* weather-vane modes. This is because the cluster of spins of a weather-vane mode must be bounded by spins pointing to the same direction. Those boundary spins inevitably involve all three sublattices if the cluster is finite. However, an A-site spin can never be in the same direction as a B-site spin if $\theta_0=\arccos(-1/2\alpha)$ is incommensurate to 2π.

There could still be nonlocal weather-vane modes involving an infinite number of spins in the thermodynamic limit. However, the number of these modes do not scale as the area of the system. In this respect, the ground state manifold of the distorted kagomé model is much less connected than that of the isotropic kagomé model. Thus, glassy behavior is more likely to happen in the distorted model.

Huse and Rutenberg studied the ground state ensemble of the isotropic kagomé antiferromagnet[15] by field theoretical and Monte Carlo methods and found that the spin-spin correlation has the $\sqrt{3}\times\sqrt{3}$ state signature but with power-law decay.

We study the classical ground state ensemble of the distorted model by measuring the ensemble-averaged spin-spin correlation. Lacking a good Monte Carlo algorithm, we use the exact enumeration result for $L\times L$ lattice with open boundary up to $L=9$. Because of the small size and possible boundary effects, we have not been able to extract the scaling form of the correlation functions. However, the result is qualitatively different from those of the isotropic kagomé antiferromagnet. For A sublattice, the correlation has a large $q=0$ (Γ-point) component. For $B(C)$ sublattice, the correlation has a large Fourier component at the M point, the midpoint of the BZ top (bottom) edge.

Based on these hints, we propose an ordering pattern as in Fig. 1. It has horizontal alternating stripes of positive (negative) chiralities. We will later call it the chirality stripe state. This pattern doubles the magnetic unit cell in the vertical direction, thus reducing the Brillouin zone (BZ), and the M point is actually equivalent to the Γ point for the reduced BZ (Fig. 1).

To further confirm this, we measured the mean square of three Fourier modes of the chirality variables $\langle m^2\rangle$: (i) the uniform pattern, corresponding to the $q=0$ (Γ point in BZ) spin configuration, with $m_\Gamma=\Sigma\eta$; (ii) the staggered pattern, corresponding to the $\sqrt{3}\times\sqrt{3}$ spin configuration of the isotropic case or K point in BZ, with $m_K=\Sigma\pm\eta$, where the two sublattices in the honeycomb chirality lattice have opposite $\pm$signs; and (iii) the chirality stripe pattern, corresponding to our proposed spin configuration (M point in BZ), with $m_M=\Sigma\pm\eta\exp(i\mathbf{k}_M\cdot\mathbf{R})$, where the $\pm$signs are the same as the staggered pattern, $\mathbf{R}$ is the position of the honeycomb unit cell, and $\mathbf{k}_M$ is the wave vector of M-point (Fig. 1).

Results are summarized in Table I. For the isotropic kagomé model, the staggered pattern mode has the largest mean-square value, while for the distorted kagomé model, the chirality stripe pattern has the largest mean-square value, which is consistent with the ensemble-averaged spin-spin correlation result. Also, from the scaling of the mean squares with system size, we conclude that there is no long-range order for chirality variables at these Fourier modes.

B. Comparison with ^{51}V NMR in volborthite

We have already noted that in contrast to classical ground states on the isotropic kagomé lattice, all ground states on the distorted kagomé lattice are disconnected from one another and require moving an infinite number of spins. Within a semiclassical viewpoint, large kinetic barriers separating the distorted kagomé ground states might lead to freezing at low temperatures. Interestingly, low-temperature NMR experiments[19] on volborthite indicate spin freezing below 1.5 K ($\sim J/60$),[20] but no such freezing is observed in the isotropic herbertsmithite.[21–24] It is tempting to attribute this difference in behavior to the difference in connectivity of classical ground states in the two cases. The vanadium atoms occupy the hexagon centers of the kagomé lattice and are hence coupled to six spin-1/2 Cu moments. Experimentally, on cooling through the glass transition temperature, there is a rapid rise of $1/T_1$, and at lower temperatures, two distinct local environments for the ^{51}V sites appear, a higher static field environment (rectangular line shape) estimated to involve 20% of spins and a lower field environment (Gaussian line shape) for the remainder. We assume that the glassy state locally resembles one of the classical ground states, and that they occur with equal probability. Then, a volume average of a local quantity in the glassy state corresponds to an ensemble average over classical ground states. Of relevance to the NMR experiments here is the distribution of exchange fields at the ^{51}V site, arising from spin configurations on the hexagons. For the nearly isotropic case $\alpha \approx 1$, three different field values (H) are possible, $H \approx 3H_{\mathrm{Cu}}$, $H \approx \sqrt{3}H_{\mathrm{Cu}}$, and $H \approx 0$, where H_{Cu} is the field from a single spin. For example, the first corresponds to a local $\sqrt{3}\times\sqrt{3}$ pattern with staggered chirality. We need to calculate the probability to find these different fields.

The authors of Ref. 19 put forward the interesting suggestion that the high field component seen in NMR corresponds to local $\sqrt{3}\times\sqrt{3}$ pattern. Their arguments though rested on properties of the isotropic kagomé model. Here, we analytically evaluate the probability distribution of different field configurations for the distorted kagomé lattice using the transfer matrix method (details in Appendix A). The probability of obtaining the $3H_{\mathrm{Cu}}$ exchange field is found to vanish in the thermodynamics limit, while that of the $\sqrt{3}H_{\mathrm{Cu}}$ is 25% and that of that the approximately zero field configuration is 75%. This is roughly consistent with the experimental observation but implies a revised value for the local moment that was obtained in Ref. 19 which assumed a local field of $3H_{\mathrm{Cu}}$. Hence, we anticipate a copper moment per site of $0.4\times\sqrt{3}=0.7$ of the full moment for small anisotropy. If the anisotropy is significant, the local field also changes, with the previous $\sqrt{3}H_{\mathrm{Cu}} \rightarrow \sqrt{(5\alpha-2)/\alpha^3}H_{\mathrm{Cu}}$ and the zero field values now being $|2-2\alpha^{-1}|H_{\mathrm{Cu}}$ (with 50% probability) and $\alpha^{-2}|\alpha-1|H_{\mathrm{Cu}}$ (with 25% probability). This suggests an upper bound for the anisotropy by requiring the local moment be less than unity, which gives $\alpha < 1.6$.

III. EFFECT OF FLUCTUATIONS ABOUT THE CLASSICAL GROUND STATES

It is well known that thermal or quantum fluctuation can lift the classical ground state degeneracy.[25] In the isotropic kagomé model, these kinds of "order-by-disorder" studies suggest that the kagomé antiferromagnet would select the $\sqrt{3}\times\sqrt{3}$ ground state,[12–15,26] namely, the staggered chirality pattern.

We study the order-by-disorder effect in the distorted kagomé model ($\alpha > 1$) by quantum and classical "spin-wave" theory. It is found that at quadratic order, the fluctuations (quantum or classical) cannot distinguish different coplanar classical ground states. One has to go beyond quadratic order of fluctuation to find order-by-disorder phenomenon.

A. Linear spin-wave theory

A classical coplanar ground state can be described by angles θ_j of classical spins with respect to a reference direction in spin space. Define a local spin axis for every site such that the S^z axis is perpendicular to the common plane of all classical spins, and the S^x axis is along the classical spin direction.

The Hamiltonian becomes

$$H = \sum_{\langle ij \rangle} J_{ij}[S_i^z S_j^z + \cos(\theta_{ij})(S_i^x S_j^x + S_i^y S_j^y) + \sin(\theta_{ij})(S_i^x S_j^y - S_i^y S_j^x)], \tag{3}$$

where $\theta_{ij} = \theta_i - \theta_j$ is the angle between classical spins on sites i and j, and the chiralities determine the sign of these angle differences.

For quantum spin-S spins, we can use the Holstein-Primakoff bosons to describe the fluctuations

$$S_i^x = S - n_i,$$

$$S_i^+ = S_i^y + iS_i^z = \sqrt{2S - n_i}\, b_i,$$

$$S_i^- = S_i^y - iS_i^z = b_i^\dagger \sqrt{2S - n_i},$$

where $n_i = b_i^\dagger b_i$ is the boson number operator.

Expanding in powers of $1/S$, the Hamiltonian becomes

$$H = E_{\mathrm{GS}} + S^{3/2}H_1 + SH_2 + S^{1/2}H_3 + H_4 + \cdots,$$

where E_{GS} is the classical ground state energy and H_n contains nth order boson creation (annihilation) operator polynomials. In fact, H_1 identically vanishes. H_2 gives the quadratic (or so-called linear) spin-wave theory,

$$H_2 = \sum_{\langle ij \rangle} H_{2,ij},$$

$$H_{2,ij} = -J_{ij}\cos(\theta_{ij})[n_i + n_j - (1/2)(b_i^\dagger + b_i)(b_j^\dagger + b_j)] - (1/2)J_{ij}(b_i^\dagger - b_i)(b_j^\dagger - b_j). \tag{4}$$

Notice that H_2 only depends on $\cos(\theta_{ij})$; then, it is identical for all classical ground state configurations (θ_{ij} can differ only by a sign between different classical ground states). Therefore, spin-wave expansion at the quadratic level cannot lift the classical degeneracy.

Dispersion of the quadratic spin wave is presented in Appendix B. One interesting result is that although the disper-

sion becomes much more complicated than that of the isotropic kagomé model, the zero-energy flatband still exists. Another strange feature is that as long as $\alpha \neq 1, \alpha > 1/2$, the "spin-wave velocity" vanishes in the direction perpendicular to the BC bonds.

B. Classical spin wave expansion and effective chirality Hamiltonian

To lift the classical degeneracy, we need to consider the "nonlinear" spin-wave theory, especially the cubic order terms H_3, because they are the lowest order terms distinct for different classical ground state configurations. Following Henley and Chan,[12] we can, in principle, derive the effective interactions between chirality variables. In the remaining part of this section, we use a different formalism by combining the idea of Henley and Chan and the classical low-temperature spin-wave expansion.[27–29]

We consider classical O(3) spins on the distorted kagomé lattice. To simplify the notations, we set the spin length S to unity. We define local spin axis as in previous section, S^z axis perpendicular to all spins and S^x axis along the classical spin. We can still use the expression [Eq. (3)] for the Hamiltonian. For classical spin, it is convenient to parametrize the fluctuation by

$$S^y = \epsilon^y, \quad S^z = \epsilon^z, \quad S^x = \sqrt{1 - (\epsilon^y)^2 - (\epsilon^z)^2},$$

and the in-plane ϵ^y and out-of-plane ϵ^z fluctuations are supposed to be small at low temperatures.

The most important contributions to the partition function comes from fluctuations around classical ground states,

$$\mathcal{Z} = Z_0^{-1} \int \mathcal{D}\mathbf{S} \exp(-\beta H) \prod_i \delta[(\mathbf{S}_i)^2 - 1]$$

$$\propto \sum_{\text{classical GS}} \int \mathcal{D}\epsilon^y \mathcal{D}\epsilon^z \exp(-\beta H) \prod_i \left(\frac{1}{S_i^x}\right),$$

where $\delta[(\mathbf{S}_i)^2 - 1]$ is the Dirac-δ function used to ensure unit spin length, and the product $\Pi(1/S_i^x)$ is the Jacobian of changing variables from O(3) spin to ϵ^y and ϵ^z. $Z_0 = (2\pi)^{3N}$ is chosen in such a way that $\mathcal{Z} \to 1$ as $\beta \to 0$ (N is the number of unit cells).

Absorb the Jacobian into the exponential and expand S^x in terms of ϵ^y and ϵ^z, then the exponent becomes

$$-\beta H = -\beta \left[H_2^y + H_2^z + H_3 + H_4 - \left(\frac{1}{2}\right) T \sum_i \xi_i + \cdots \right],$$

where $-(1/2)T\Sigma_i[(\epsilon_i^y)^2 + (\epsilon_i^z)^2]$ comes from the Jacobian, and to simplify the notation, we define $\xi_i = (\epsilon_i^y)^2 + (\epsilon_i^z)^2$. Then,

$$H_2^y = \sum_{\langle ij \rangle} J_{ij} \cos(\theta_{ij}) \{\epsilon_i^y \epsilon_j^y - (1/2)[(\epsilon_i^y)^2 + (\epsilon_j^y)^2]\},$$

$$H_2^z = \sum_{\langle ij \rangle} J_{ij} \epsilon_i^z \epsilon_j^z - \left(\frac{1}{2}\right) J_{ij} \cos(\theta_{ij}) [(\epsilon_i^z)^2 + (\epsilon_j^z)^2],$$

$$H_3 = -\left(\frac{1}{2}\right) \sum_i \sum_j J_{ij} \sin(\theta_{ij}) \epsilon_i^y \xi_j,$$

$$H_4 = \left(\frac{1}{8}\right) \sum_{\langle ij \rangle} J_{ij} \cos(\theta_{ij}) (\xi_i^2 + 4\xi_i \xi_j + \xi_j^2). \tag{5}$$

Again, the quadratic terms are identical for all classical ground states.

We can rescale ϵ^y and ϵ^z by $\sqrt{\beta}$ to absorb β into H_2^y and H_2^z. Defining $\tilde{\epsilon}^y = \sqrt{\beta}\epsilon^y$ and $\tilde{\epsilon}^z = \sqrt{\beta}\epsilon^z$, then the exponent becomes

$$-\beta H = -\tilde{H}_2^y - \tilde{H}_2^z - \sqrt{T}\tilde{H}_3 - T\tilde{H}_4 - \mathrm{O}(T^2),$$

where $\tilde{H}_2^{y,z}$ and $\tilde{H}_3$ are obtained by replacing ϵ^y, ϵ^z by $\tilde{\epsilon}^y$, $\tilde{\epsilon}^z$ in the formulas of H_2^y, H_2^z, and H_3, respectively. $\tilde{H}_4$ combines the original quartic order term H_4 and the lowest order term from the Jacobian, and we have set the Boltzmann constant $k_B = 1$. Since higher-than-quadratic order terms are controlled by temperature, we can do a controlled perturbative expansion in powers of the small parameter T.

As the first approximation, we may keep only $\tilde{H}_2^y$ and $\tilde{H}_2^z$ for very low T. Solution of the quadratic theory is presented in Appendix C. The out-of-plane fluctuation $\tilde{\epsilon}^z$ has a flat zero-energy band, which is consistent with the mode-counting argument of Moessner and Chalker.[17] The in-plane fluctuation has the "Goldstone" mode at wave vector $\mathbf{k} = 0$. However, since this is a classical theory, the dispersion around the Goldstone mode is quadratic.

C. Effective chirality Hamiltonian

Now we can formally write down an expansion for small T. Define $\mathcal{Z}_0 = \int \exp(-\tilde{H}_2^y - \tilde{H}_2^z) \mathcal{D}\tilde{\epsilon}^y \mathcal{D}\tilde{\epsilon}^z$. Remember that $\mathcal{Z}_0$ is the same for all classical ground states we are perturbing. The free energy f per unit cell for fluctuations around one classical ground state is

$$f = (1/N)E_{\text{GS}} - 3T \ln T - (1/N)T \ln \mathcal{Z}_0 - (1/2)T^2 \langle (\tilde{H}_3)^2/N \rangle_0 + T^2 \langle \tilde{H}_4/N \rangle_0 + \mathrm{O}(T^3), \tag{6}$$

where N is the number of unit cells, and $\langle \mathcal{A} \rangle_0$ means the expectation value in the quadratic theory, i.e., $\langle \mathcal{A} \rangle_0 = \mathcal{Z}_0^{-1} \int \mathcal{A} \exp(-\tilde{H}_2^y - \tilde{H}_2^z) \mathcal{D}\tilde{\epsilon}^y \mathcal{D}\tilde{\epsilon}^z$. Since $\mathcal{Z}_0$ and $\tilde{H}_4$ are identical for all classical ground states, difference at T^2 order comes from the $\langle (\tilde{H}_3)^2/N \rangle_0$ term. Remember that each term in H_3 contains a $\sin(\theta_{ij})$, the sign of which is determined by the chirality of the triangle containing the bond $\langle ij \rangle$. Therefore, $\langle (\tilde{H}_3)^2/N \rangle_0$ will generate effective chirality-chirality interactions $J_{ij}\eta_i\eta_j$ for each pair of chirality variables η_i and η_j. Details about the calculation of the chirality interactions are presented in Appendix C.

There are two technical obstacles for this order-by-disorder analysis: (i) The flat zero-energy band will make the two-$\tilde{\epsilon}^z$ correlation function diverge and (ii) the Goldstone mode will make the two-$\tilde{\epsilon}^y$ correlation function diverge. Both (i) and (ii) will make $\langle (\tilde{H}_3)^2/N \rangle_0$ divergent.

To proceed, we add a term $J^z \Sigma_i (S_i^z)^2$ in the Hamiltonian. This can be thought as a single-ion anisotropy term disfavoring out-of-plane fluctuation. The flat zero-energy band will

TABLE II. Effective chirality couplings J_{1-6} (see Fig. 11) divided by T^2 for $J^z=0.1$ and $J^y=0.01$. Positive number means antiferromagnetic coupling.

α	J_{1v}	J_{1h}	J_{2v}	J_{2h}	
1	0.9702	0.9702	0.2614	0.2614	
1.5	1.8231	−0.3340	−0.01294	0.8895	
α	J_{3v}	J_{3h}	J_{4u}	J_{4m}	J_{4d}
1	0.1916	0.1916	0.002661	0.002661	0.002661
1.5	0.4318	0.3631	0.04897	−0.2770	0.007420
α	J_{5v}	J_{5h}	J_{6v}	J_{6h}	
1	0.002924	0.002924	0.002914	0.002914	
1.5	−0.06089	0.01172	−0.03724	0.1996	

be shifted to a positive value and no longer produce divergence. We also need to cure the divergence from the in-plane Goldstone mode. However, no natural interaction can do this job. Therefore, we add an artificial mass term $J^y\Sigma_i(\epsilon_i^y)^2$ to the Hamiltonian, which gives the Goldstone mode a small gap, or can be thought as an infrared cutoff. Eventually, we would like to take the limit J^z, $J^y\to 0$. More detailed renormalization group (RG) treatment has been done by Brezin and Zinn-Justin.[27]

To check consistency, we first calculated the effective chirality interactions for $\alpha=1$ kagomé model. The interactions are antiferromagnetic and seems to be short ranged (see Table II in Appendix C). Because the nearest-neighbor chirality antiferromagnetic coupling dominates, the staggered chirality pattern (namely, the $\sqrt{3}\times\sqrt{3}$ spin configuration) is selected, which is consistent with all previous order-by-disorder studies for the isotropic kagomé model. This selection is independent of J^z and J^y for the range of parameters we studied.

The $\alpha>1$ case is more delicate. It seems that the chirality interaction is not short-ranged (see Table II in Appendix C), and the selection of chirality pattern is more sensitive to J^z and J^y. We have calculated chirality interactions up to sixth neighbor, with $J^y=0.01$ as the smallest value we can use and for various J^z, and α. A rough picture (Fig. 3) is that for α close to unity or small J_z, the staggered chirality pattern

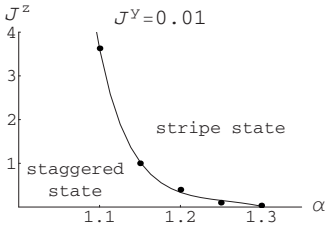

FIG. 3. Phase diagram obtained from classical spin-wave order-by-disorder analysis with $J^y=0.01$ (artificial gap for in-plane fluctuation). J_z is the single-ion anisotropy. For large α or J^z, the chirality stripe pattern is selected. Dots are calculated boundary points, and the line is a guide for the eye. Weak interlayer couplings are assumed to stabilize true long-range order.

(analog of the $\sqrt{3}\times\sqrt{3}$ spin configuration of the isotropic kagomé model) is still favored, but in the other part of the parameter space, our proposed chirality stripe state is selected. One should be aware that this picture may still depend on the unphysical parameter J^y, and including further neighbor chirality interactions may also modify the phase boundary.

We have also tried to use this approach for $\alpha<1$ case. However, the selection of ground state is much more sensitive to the unphysical parameters and the number of chirality-chirality couplings we include. We decide to leave this part for more detailed studies in the future.

IV. LARGE-*N* APPROXIMATION

Another way to study (anti)ferromagnet is to generalize classical O(3) spin to O(n) spin. At $n\to\infty$ limit, the theory can be solved exactly by saddle point approximation. One can also calculate $1/n$ corrections systematically. The saddle point approximation is supposed to be good for high-temperature disordered phase. As temperature decreases, one can usually decide at which wave vector the long-range order is developed by looking at the position of the lowest "excitation" energy, or the lowest eigenvalue(s) of the inverse of the spin correlation function matrix.

For the isotropic kagomé model, the lowest excitation is wave vector independent in the saddle point solution. For distorted kagomé ($\alpha>1$) model, the lowest excitation is degenerate on a line in momentum space. We have to include $1/n$ correction to determine the possible ordering wave vector uniquely. However, for $\alpha<1$, the $q=0$ wave vector is selected at the saddle point level.

A. Saddle point solution and line degeneracy for distorted kagomé lattice

The model we use is the O(n) spin antiferromagnet on the distorted kagomé lattice,

$$H=\sum_{\text{triangles}}\sum_{a=1}^{n}(S_A^aS_B^a+\alpha S_B^aS_C^a+S_C^aS_A^a), \tag{7}$$

with constraints $\Sigma_{a=1}^n(S_i^a)^2=1$. We rescale all spins and β by $\tilde{S}_i^a=\sqrt{n}S_i^a$ and $\tilde{\beta}=\beta/n$. The partition function becomes

$$\mathcal{Z} = Z_0^{-1} \int \left(\prod_{i,a} d\tilde{S}_i^a \right) \exp(-\tilde{\beta}\tilde{H}) \prod_i \delta\left[n - \sum_a (\tilde{S}_i^a)^2 \right],$$

where $Z_0 = [n^{n/2}\pi^{n/2}/\Gamma(n/2)]^{3N}$ such that $\mathcal{Z} \to 1$ as $\beta \to 0$, N is the number of unit cells, and $\tilde{H}$ is the Hamiltonian H with S directly replaced by $\tilde{S}$. In the remainder of this section, we will write $\tilde{S}$, $\tilde{H}$, and $\tilde{\beta}$ as S, H, and β, respectively. We will write $\mathcal{D}\mathbf{S}$ instead of $\Pi_{i,a} dS_i^a$.

Using the fact that

$$\delta(x) = \int_{-\infty}^{\infty} \frac{d\lambda_i}{2\pi} \exp[(i\lambda_i + \mu_i)x],$$

where λ_i is a real dummy variable and μ_i is an arbitrary real parameter to be determined later by the saddle point condition, we can rewrite the partition function as

$$\mathcal{Z} = Z_0^{-1} \int \mathcal{D}\mathbf{S}\mathcal{D}\lambda \exp\left\{ -\beta H + \sum_i \tilde{\lambda}_i \left[n - \sum_a (S_i^a)^2 \right] \right\}$$

$$= Z_0^{-1} \int \mathcal{D}\mathbf{S}\mathcal{D}\lambda \exp\left[-\sum_{a,i,j} S_i^a M_{ij} S_j^a + \sum_i n\tilde{\lambda}_i \right], \quad (8)$$

in which $M_{ij} = (i\lambda_i + \mu_i)\delta_{ij} + \beta J_{ij}/2$ is a symmetric matrix, $\tilde{\lambda} = i\lambda + \mu$, and $\mathcal{D}\lambda = \Pi_i [d\lambda_i/(2\pi)]$. Integration over S_i^a gives

$$\mathcal{Z} = Z_0^{-1} \pi^{3nN/2} \int \mathcal{D}\lambda \det(M)^{-n/2} \exp\left[\sum_i n(i\lambda_i + \mu_i) \right].$$

Now, the saddle point condition is

$$\frac{\partial}{\partial \mu_i} \ln \det(M) = 2, \quad \forall\, i.$$

Let us assume that the saddle point solution has all lattice symmetries, e.g., translational invariance. Then, μ_i depends only on which sublattice the site i belongs to. Furthermore, because the B and C sublattices are equivalent, we have $\mu_B = \mu_C$.

Assuming translationally invariant μ_i, the matrix M_{ij} can be block diagonalized by Fourier transformation. $\det(M) = \Pi_{\mathbf{k}} \det[M(\mathbf{k})]$, where $M(\mathbf{k})$ is a 3×3 matrix,

$$M(\mathbf{k}) = \begin{pmatrix} \mu_A & \beta\cos(k_3/2) & \beta\cos(k_2/2) \\ \beta\cos(k_3/2) & \mu_B & \alpha\beta\cos(k_1/2) \\ \beta\cos(k_2/2) & \alpha\beta\cos(k_1/2) & \mu_C \end{pmatrix},$$

with $k_i = \mathbf{k}\cdot\mathbf{e}_i$ ($k_3 = -k_1 - k_2$). The saddle point condition becomes

$$\left(\frac{1}{N}\right) \sum_{\mathbf{k}} \frac{\partial}{\partial \mu_X} \ln \det[M(\mathbf{k})] = 2, \quad X = A, B, C,$$

and in the thermodynamic limit $N \to \infty$, the sum becomes a integral over the Brillouin zone, $(1/N)\Sigma_{\mathbf{k}} \to \int_0^{2\pi}\int_0^{2\pi} dk_1 dk_2/(2\pi)^2$.

This saddle point equation cannot be solved analytically. However, when β is small, we can expand it in terms of β and obtain a high-temperature series for μ_X. The result is

$$2\mu_A = 1 + 4\beta^2 - 4\alpha\beta^3 + \cdots, \quad (9a)$$

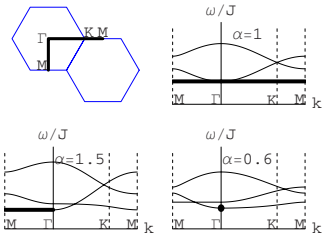

FIG. 4. (Color online) Dispersion ω of the O(n) model in the saddle point approximation along certain high symmetry directions (shown in the first panel) for three different α at $\beta = 0.2$. The lowest eigenvalue(s) are shown with bold lines (dot).

$$2\mu_{B,C} = 1 + 2(\alpha^2 + 1)\beta^2 - 4\alpha\beta^3 + \cdots. \quad (9b)$$

We notice that $\mu_{B,C} > \mu_A$ for $\alpha > 1$, which leads to a degenerate line of lowest excitation in the saddle point approximation. This high-temperature (small β) series can be extended to intermediate temperature (β) by Padé approximation.

After solving μ_X, we can solve the "dispersion," or the eigenvalues of $M(\mathbf{k})$. Dispersion along certain high symmetry directions is shown in Fig. 4. Note that for $\alpha < 1$, the lowest eigenvalue is uniquely determined at $\mathbf{k} = 0$. However, for $\alpha > 1$, the lowest eigenvalue is degenerate on the $k_1 = 0$ line, or the vertical Γ-M line in the BZ. Finally, for $\alpha = 1$, the lowest eigenvalue is degenerate over the entire BZ.

To decide the ordering wave vector uniquely, we must consider $1/n$ correction for $\alpha \geq 1$ cases. Before presenting that in the next section, we show the calculated elastic neutron scattering intensity (Fig. 5) $[\Sigma_{X,Y}(M^{-1})_{XY}]^2$ of the saddle point solutions for four different α with relatively high temperature $\beta = 0.2$ (summation is over $X, Y = A, B, C$). We emphasize that the maximum appearing in the elastic neutron scattering intensity does not directly correspond to the possible long-range-order wave vector.

B. Lifting the line degeneracy of $\alpha > 1$: $1/n$ correction

To lift the degeneracy of the lowest excitations of the saddle point approximation, we have to include fluctuations around the saddle point.

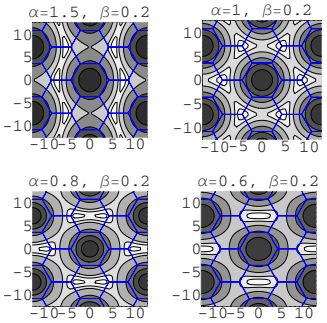

FIG. 5. (Color online) Predicted elastic neutron scattering intensity for distorted kagomé model, obtained from the saddle point solutions at $\beta = 0.2$ for four different α. Hexagons are BZ borders. Darker regions have lower intensities. The $\alpha > 1$ case shows quasi-1D feature.

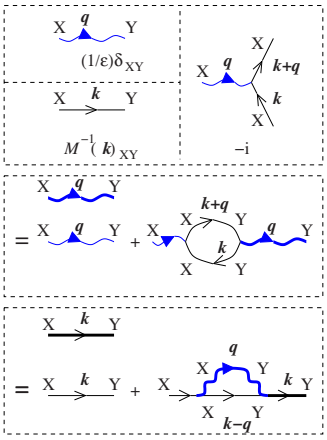

FIG. 6. (Color online) Feynman rules for calculating $1/n$ corrections of O(n) model. O(n) indices are omitted. X and Y are sublattice indices. The first panel contains free propagators and the only vertex in the theory. Straight lines represent the spin propagator. The second panel is the one-loop Dyson equation [Eq. (10)] for the λ propagator. The third panel is the one-loop Dyson equation [Eq. (11)] for the spin propagator. Thick lines are full propagators.

We have three $\lambda_{X,\mathbf{k}}$ fields and $3n$ $S^a_{X,\mathbf{k}}$ fields in the action, where X is the sublattice index and a is the O(n) index of spin. The Green's function of the spins with the same O(n) indices is a 3×3 matrix. Under the saddle point approximation, it is $G^{(0)}_{S,ab,XY}(\mathbf{k})=[M(\mathbf{k})]^{-1}_{XY}\delta_{ab}$, where $X,Y=A,B,C$ for three sublattices and a,b are O(n) indices. We need the correction to this Green's function by the fluctuations of λ around zero. From Eq. (8), we see that there is a three-leg vertex between λ and S^a of the form $-i\lambda_i(S^a_i)^2$.

The Feynman rules and Dyson equations are summarized in Fig. 6. Notice that the three-leg vertex preserves sublattice index for all fields and also O(n) index for the spins. There is no free propagator for λ fields in the original theory. To make the perturbative expansion well defined, we add a term $+\Sigma_i\epsilon(\lambda_i)^2$ to the Hamiltonian, which corresponds to a free propagator $(1/\epsilon)\delta_{XY}$. Finally, we will take the $\epsilon\to 0$ limit.

The one-loop Dyson equation for the propagator of λ is shown in Fig. 6. The inverse of the Green's function at one-loop level is

$$[G^{-1}_{\lambda}(\mathbf{k})]_{XY}=(\epsilon)\delta_{XY}-\Gamma_{\lambda,XY}=-\Gamma_{\lambda,XY}, \tag{10}$$

where Γ_λ is the self-energy of λ (the loop diagram in the second panel of Fig. 6). Here, we have taken the $\epsilon\to 0$ limit,

$$\Gamma_{\lambda,XY}=\sum_a(-i)^2\int_{\mathrm{BZ}}d^2\mathbf{q}G^{(0)}_{S,aa,XY}(\mathbf{k}+\mathbf{q})G^{(0)}_{S,aa,YX}(\mathbf{q})$$

$$=-n\int_{\mathrm{BZ}}d^2\mathbf{q}[M^{-1}(\mathbf{k}+\mathbf{q})]_{XY}[M^{-1}(\mathbf{q})]_{YX}.$$

There is no summation over sublattice indices X,Y on the right-hand side. $\int_{\mathrm{BZ}}d^2\mathbf{q}$ is the normalized integral over the entire BZ. Since the summation over O(n) index a becomes a factor of n, the one-loop λ propagator is of the order $1/n$.

We use this one-loop λ propagator to calculate the one-loop correction to the spin propagator,

$$[G^{-1}_{S,aa}(\mathbf{k})]_{XY}=[M(\mathbf{k})]_{XY}-\Gamma_{S,aa,XY}, \tag{11}$$

where $\Gamma_{S,XY}$ is the self-energy of spins (the loop diagram in the third panel of Fig. 6).

$$\Gamma_{S,aa,XY}=(-i)^2\int_{\mathrm{BZ}}d^2\mathbf{q}G^{(0)}_{S,aa,XY}(\mathbf{k}-\mathbf{q})G_{\lambda,XY}(\mathbf{q}).$$

Again there is no summation over X,Y on the right-hand side.

These integrals cannot be evaluated exactly. Instead, we use the high-temperature (small β) expansion to get analytical result. We found that up to β^7 order, the one-loop correction does not qualitatively change the form of $G^{-1}_{S,aa}(\mathbf{k})$. It has similar wave vector dependence of the inverse free propagator $M(\mathbf{k})$; therefore, the line degeneracy of $\alpha>1$ model and the degenerate band of $\alpha=1$ model cannot be lifted at β^7 order.

However, at β^8 order, a qualitatively distinct correction appears. The self-energy (the loop diagram) contains a term

$$(1/n)\beta^8 C\begin{pmatrix} 0 & \alpha\cos\left(\frac{k_{12}}{2}\right) & \alpha\cos\left(\frac{k_{13}}{2}\right) \\ \alpha\cos\left(\frac{k_{21}}{2}\right) & 0 & \frac{\mu_{BC}}{\mu_A}\cos\left(\frac{k_{23}}{2}\right) \\ \alpha\cos\left(\frac{k_{31}}{2}\right) & \frac{\mu_{BC}}{\mu_A}\cos\left(\frac{k_{32}}{2}\right) & 0 \end{pmatrix},$$

where $k_{ij}=k_i-k_j$ and a constant $C=\alpha^2/(64\mu_A^2\mu_{BC}^5)$. This looks like a next-neighbor ferromagnetic coupling.

For $\alpha>1$ model, we have a degenerate line $k_1=0$ at the saddle point level. This $(1/n)\beta^8$ correction will favor $k_2=\pi$, which is the M point in the BZ. For $\alpha=1$ model, we have a degenerate band in the saddle point approximation. This $(1/n)\beta^8$ correction will favor $k_1=k_2=4\pi/3$, which is the K point in the BZ, corresponding to the $\sqrt{3}\times\sqrt{3}$ spin configuration.

We notice that a previous high-temperature series expansion study[30] also lifts the degeneracy of the kagomé O(n) model at β^8 order. Their result contains, in some sense, corrections to all orders of $1/n$ but does not have a simple analytical form. Our simpler analytic method (expanding in both $1/n$ and β) is complementary to their linked-cluster series expansion study and our results are consistent with theirs in the region of overlap.

V. QUANTUM LIMIT: EXACT DIAGONALIZATION AND SLAVE PARTICLE MEAN FIELD THEORIES

We have performed exact diagonalization on small lattices of spin-1/2 moments to study the effect of distortions in the kagomé model. We used the open source ALPS library and applications[31] on an office computer. Two different kinds of results are presented: the nature of the ground state and low lying excitations and the thermodynamics (specific heat and magnetic susceptibility). The latter requires knowing all ei-

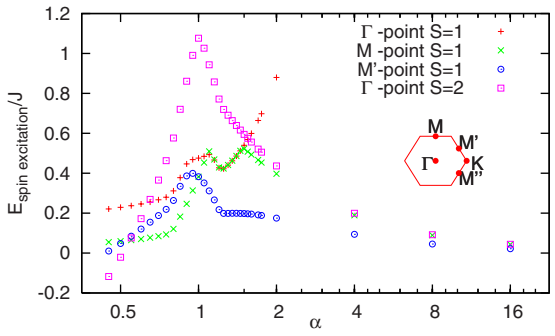

FIG. 7. (Color online) spin excitation energies at different wave vectors from the exact diagonalization study (12 sites: 2×2 unit cell system with periodic boundary condition). Energy is measured from the lowest singlet state (ground state for $\alpha>1/2$). Other spin excitations, $S>2$ at any wave vector or $S=2$ away from the Γ point, have much high energies than the ones plotted.

genvalues of the Hamiltonian and is hence restricted to small system sizes of 12 sites (2×2 unit cells) with periodic boundary conditions. Based on previous studies,[32] we believe that this small system can still produce qualitatively correct high-temperature properties. For the former, we study system sizes up to 24 sites (4×2).

Before discussing the results of exact diagonalization for the low lying eigenstates, let us briefly recall the expectation from the semiclassical picture developed so far.

(1) For $\alpha<1/2$, a collinear ferrimagnetic state with a magnetization of $1/2$ per unit cell is expected.

(2) For $\alpha>1$, the ferrimagnetic chirality stripe state is expected, which implies a net spin in the ground state and low energy spin excitations at the M point as shown in the inset of Fig. 7.

(3) For $1/2<\alpha<1$, we do not have a firm expectation from semiclassics; however, the large-n saddle point solution seems to favor a $q=0$ state, which would also be ferrimagnetic.

Numerically, we find that the first prediction is remarkably well obeyed even in this extreme quantum limit. On decreasing α, the ground state is found to have nonzero total spin. Moreover, this is found to happen precisely below $\alpha=1/2$. The ground state moment is also exactly what is expected, for example, it is $S=2$ for the 2×2 lattice and $S=3$ for the 3×2 lattice.

For $\alpha>1/2$, the comparison is less clear. For example, the ground state is a spin singlet on lattice sizes up to 24 sites. However, there is a clear tendency of the $S=2$ state at the Γ point to drop in energy on moving away from the isotropic kagomé point as seen in Fig. 7, indicating perhaps a tendency to develop a net moment. On the other hand, while the spin gap may be expected to be soft along the M point (the wave vector for the chirality state) for $\alpha>1$, it turns out that the M point is actually not the location of the lowest spin carrying excitation—which instead occurs at different wave vectors, the M' (and equivalent M'') locations in the case of 2×2 system. Similarly, for the 4×2 system, the $S=1$ excitation energy at the M point is higher than those at the M' and M'' points (the latter two are inequivalent on this lattice). Moreover, the lowest $S=1$ excitation occurs at the M'' point.

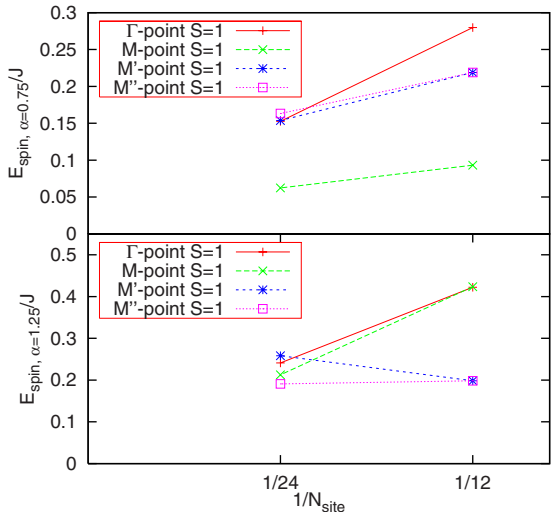

FIG. 8. (Color online) Spin excitation energies at the high symmetry points (see inset in Fig. 7 for definition) vs number of sites, for $\alpha=0.75$ and 1.25, for 12-site and 24-site systems. Due to the geometry of the 24-site (4×2 unit cell) lattice, the M' and M'' points are not equivalent. Lines are guides for the eye.

It should be noted though that the $S=1$ excitation energy at the M point decreases rapidly from the 12-site to the 24-site lattice (Fig. 8) and might end up being the lowest spin excitation at larger system sizes. Paradoxically, in the $1/2<\alpha<1$ limit, the M point is the location of the lowest spin carrying excitation, both in the 12 and 24 sized systems we studied. We therefore have to leave the question of the validity of the semiclassical "chirality stripe" picture in the extreme quantum limit open to future systematic numerical studies on bigger systems. Finally, we note that as in the isotropic kagomé case, we have observed singlet excitations inside the spin gap (the energy of the lowest excitation with nonzero spin).

Thermodynamics. The magnetic dc susceptibility and specific heat results for several different α are presented in Fig. 9. In both figures, the temperature has been rescaled by the average coupling $J_{\text{average}}=(2+\alpha)/3$ for each curve, and χ is also rescaled accordingly. For high temperatures ($T>0.2J_{\text{average}}$), the dc susceptibilities for different α converge to the $\alpha=1$ result. The positions of the broad maxima in the specific heat curves are also more or less the same for different α. Therefore, we conclude that the anisotropy does not induce qualitative difference in these two macroscopic observables for high enough temperature (e.g., $T>0.2J_{\text{average}}$).

Slave particle approaches. Other theoretical approaches can also be used to attack the problem directly from the quantum limit. These methods have been applied to the isotropic kagomé lattice and can be utilized to study the effect of distortion. The Schwinger boson technique [large-N Sp(N) approach] has been used to study the volborthite lattice recently,[33] where, for not too large spatial anisotropy, the $\sqrt{3}\times\sqrt{3}$ state was found to persist, although the ordering wave vector is shifted to an incommensurate value (the staggered chirality pattern remains the same). Fermionic slave particle representation of the spins[34] as well as the dual vor-

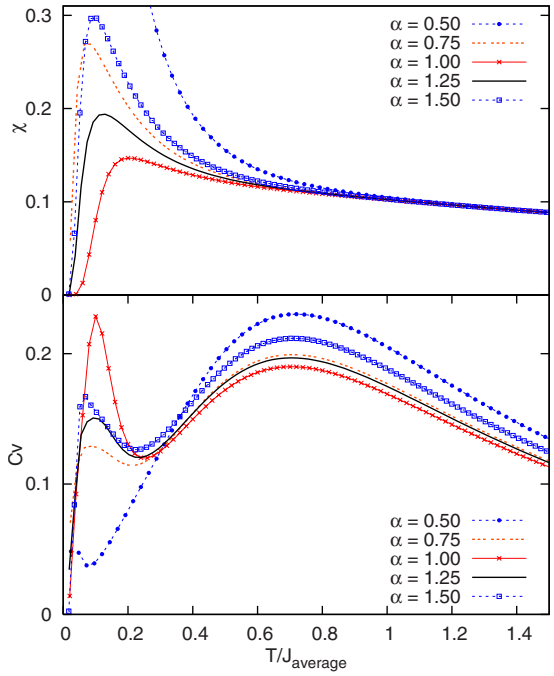

FIG. 9. (Color online) Susceptibility χ and specific heat C_v from the exact diagonalization study (2×2 unit cell system, 12 spins, with periodic boundary condition). Temperature is rescaled by the average coupling $J_{\text{average}}=(2+\alpha)/3$ for each curve. The susceptibilities of different $\alpha>0.5$ converge to the $\alpha=1$ result even at moderate temperatures. The positions of specific heat maxima at around $T/J_{\text{average}}=2/3$ are consistent between different α values.

tex formulation[35] have recently been used to study the isotropic kagomé lattice in connection to herbertsmithite. Extending these studies to the volborthite lattice should be interesting. For example, the Dirac fermions in the proposal of Ref. 34 would remain massless on the distorted lattice as well, since the mass term is prohibited by the translational and time reversal symmetries that remain intact.

VI. CONCLUSIONS

We have studied the distorted kagomé model by several approaches. First, we proved that the classical degeneracy is reduced from an extensive one (of the isotropic kagomé model) to a subextensive one. As a result, we found that the ground state ensemble is much less connected in the distorted kagomé model compared to the isotropic case. One has to change an infinite number of spins (in the thermodynamic limit) in order to move from one classical coplanar ground state to another. This could result in a greater tendency toward glassy behavior and may be consistent with the fact that spin freezing was observed (not observed) in volborthite (herbertsmithite). We then studied the properties of the ground state ensemble by enumeration and transfer matrix methods. Using transfer matrix method we calculated the probability of different local spin configurations and showed that this consideration may provide an explanation of the low-temperature NMR data in volborthite.

We then studied how this remaining degeneracy can be lifted by two refinements of various approaches to the classical problem. In particular, we used a low-temperature classical spin-wave expansion to compute the effective chirality interactions which lead to a preferred ordering pattern. We also studied the large-n $O(n)$ model in the saddle point approximation and with $1/n$ corrections, the latter being performed in conjunction with a high-temperature expansion. Our results for the isotropic case $\alpha=1$ are consistent with previous order-by-disorder studies for the isotropic kagomé model, i.e., $\sqrt{3}\times\sqrt{3}$ state is selected. However, for $\alpha>1$, both classical approaches we pursued point to a possible long-range-order pattern different from that of the isotropic kagomé model. The resulting "chirality stripe state" doubles the magnetic unit cell, has a Fourier component at the M point in the Brillouin zone, and has a net magnetic moment (Fig. 1). Of course, this classical 2D system cannot develop a long-range order at any finite temperature, but in the presence of weak inter layer couplings, the ordering pattern we propose is the most reasonable candidate if magnetic long-range order sets in. Exact diagonalization studies of small systems showed that the specific heat and susceptibility for different values of α do not vary much at intermediate temperatures upon the change of the anisotropy parameter α.

Shortly after completion of this work, there appeared another paper[37] studying the same lattice but via the Sp(N) large-N treatment and perturbation theory. Their analysis of the degree of classical degeneracy is in agreement with our result.

ACKNOWLEDGMENTS

We thank Doron Bergmann, Leon Balents, and John Hopkinson for useful discussion. We acknowledge support from the Hellman Family Faculty fund, LBNL DOE-504108 (F.W. and A.V.), the NSERC of Canada, Canadian Institute of Advanced Research, Canada Research Chair Program, KRF-2005-070-C00044, and Miller Institute for Basic Research in Science at University of California at Berkeley (Y.B.K.). Some part of this work was done at the Kavli Institute for Theoretical Physics at University of California at Santa Barbara and is supported in part by the NSF Grant No. PHY05-51164.

APPENDIX A: TRANSFER MATRIX SOLUTION OF THE CLASSICAL GROUND STATE DEGENERACY OF THE DISTORTED KAGOMÉ MODEL

In this appendix, we derive the asymptotic formula of the classical ground state degeneracy in the distorted kagomé model and also establish rigorous upper and lower bounds to show that the degeneracy is subextensive. We also study the probability of various local hexagon configurations in the ground state ensemble of the distorted kagomé model, which is related to NMR studies of the volborthite.[19]

We stretch the honeycomb chirality lattice horizontally to make a topologically equivalent "brickwall" lattice (Fig. 10). Chiralities are Ising variables on the vertices. For simplicity of derivation, we use a different, less symmetric geometry

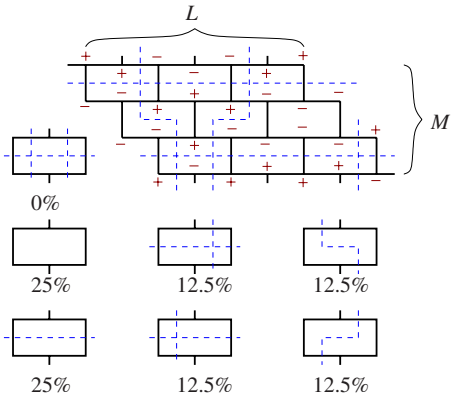

FIG. 10. (Color online) brickwall lattice for the transfer matrix study in Appendix A. Seven possible single brick configurations and their probabilities in the thermodynamic limit are presented.

other than the geometry used for enumeration study in the main text. The lattice consists of M rows of "bricks," and each row contains L bricks. We will establish the upper and lower bounds, 4^{M+L} and 2^{M+1}, for open boundary condition and the asymptotic formula 2^{M+L} for periodic boundary condition in the thermodynamic limit.

It is better to represent the states of the Ising chirality variables by domain wall configurations (Fig. 10). As in all Ising systems, the number of Ising configurations is two times the number of domain wall configurations. All possible domain wall configurations within a brick is given in Fig. 10. Number below each brick configuration is the probability of that local configuration in a lattice with periodic boundary condition in the thermodynamic limit, to be derived later.

There are several important observations:

(a) If there is a horizontal domain wall crossing, one of the vertical edges of the brickwall, this domain wall must extend through the entire lattice, cutting the entire row of bricks.

(b) The number of vertical domain walls cutting a horizontal line in the brickwall is conserved from line to line.

(c) Whether there is a horizontal extended domain wall in the row of bricks or not completely determines the propagation of vertical domain walls from the upper line to the lower line.

(d) If there are two vertical domain walls in the same brick in the upper line (we call this a "collision" of two vertical domain walls), then there must be a horizontal extended domain wall in the row of bricks, and we have only one choice for the vertical domain wall configuration on the lower line. Otherwise, for a given vertical domain wall configuration on the upper line, we have two choices on the lower line.

(e) Vertical domain walls do not cross each other.

We can obtain an upper bound for the number of chirality configurations by the following considerations for a lattice with open boundary condition: (i) The vertical domain wall configurations on the topmost line give 2^{2L} choices. (ii) The horizontal extended domain walls give a factor of *at most* 2^M. (iii) On each row of bricks except for the first row, there *could* be one additional Ising degree of freedom depending on whether there is a vertical domain wall entering from the top-right edge of the rightmost brick (an example of entering vertical domain wall is given in Fig. 10—the third row from top). This is at most a factor of 2^{M-1}. Combining all these factors, we get an upper bound 4^{M+L} for chirality configurations on the $L\times M$ open boundary lattice.

We can easily get a subextensive lower bound for open boundary condition by considering the case that there is no vertical domain wall. Then, we have 2^M domain wall configurations via the M possible horizontal extended domain walls. Thus, a lower bound of the number of chirality configurations is 2^{M+1}.

Now, we impose the periodic boundary condition on an $L\times M$ brickwall. Strictly speaking, the periodic boundary condition will introduce two additional nonlocal constraints on the chirality variables, and it will impose constraints on the total number of vertical domain walls (must be even) and also horizontal domain walls. They are not supposed to change the asymptotic behavior and we ignore them for simplicity.

Define the transfer matrix T_{xy}, where x and y label the vertical domain wall configurations on the upper and lower line of a row of bricks, respectively. T_{xy} is the number of ways that vertical domain walls in x can propagate downward to y. Some examples are as follows: (i) x is the configuration where there is no vertical domain wall in a line, and then the only y satisfying $T_{xy}\neq 0$ is $y=x$ =(no vertical domain wall) and $T_{xx}=2$ because there could be one, or no, extended horizontal domain wall in between, which should be counted as two different ways of propagation. (ii) x is the configuration where there are vertical domain walls on every edge of the upper horizontal line, and then $T_{xx}=1$ because there must be one extended horizontal domain wall in between and $T_{xy}=0$, $\forall y\neq x$.

The number of domain wall configurations is the trace of the Mth power of the $2^{2L}\times 2^{2L}$ transfer matrix T, which equals the sum of the Mth powers of all eigenvalues λ of T, $\mathrm{Tr}(T^M)=\Sigma_\lambda \lambda^M$. From the previous observations (c) and (d), we have $\Sigma_y T_{xy}\leqslant 2$. Therefore, all eigenvalues have absolute values smaller than or equal to 2. This provides an upper bound 2^{2L+M} for domain wall configurations.

Taking the thermodynamic limit $M\to\infty$, with L large but finite, then the trace $\mathrm{Tr}(T^M)$ reduces to the sum of the Mth power of the largest eigenvalues (it is 2 and can be degenerate), $\Sigma_{\lambda=2}2^M$. Now, we want to construct all eigenvectors corresponding to eigenvalue 2. The property of the ground state ensemble is dominated by these eigenvectors in the thermodynamic limit.

Suppose a_x is a (left) eigenvector with the eigenvalue 2, $\Sigma_x a_x T_{xy}=2a_y$. Then, we have the following two properties: (i) $a_x\geqslant 0$, $\forall x$, which comes from the fact that $T_{xy}\geqslant 0$; and (ii) $a_x=0$ for x containing a collision, which comes from observation (d).

If there is no collision in x, but there is one vertical domain wall crossing the top-left horizontal edge of one brick, and one of its neighboring vertical domain wall crosses the top-right horizontal edge of another brick, we can always bring those two vertical domain walls together to make a collision by propagating them downward (an example is shown in Fig. 10). Therefore, we must have $a_x=0$ for this

kind of x, which contains both vertical domain walls crossing top-left and top-right edges of some bricks.

Now, we can construct all eigenvectors with the largest eigenvalue (2). Take an x containing vertical domain walls crossing only the top-left edges of some bricks. It can propagate to the next line without change, or shifted by one-half of the lattice constant. By translating this x on the line (with periodic boundary condition) by multiples of half lattice constant, we find a connected subspace of the state space, denoted by span (x). Then, $a_y=1$, $\forall y \in \text{span}(x)$, is the (not normalized) eigenvector with the largest eigenvalue (2) in this subspace (by Perron-Frobenius theorem, this eigenvector is unique in this subspace).

The degeneracy of the largest eigenvalues (2) equals the number of distinct subspaces constructed as in the previous paragraph, or the number of inequivalent x with only the top-left-edge vertical domain walls (inequivalent under translation). This is still a nontrivial combinatorial problem, but we have a rough upper bound 2^L and a lower bound $2^L/L$. Combining all previous considerations, we have the asymptotic form of the number of configurations 2^{M+L}.

Now, we have, in principle, all the eigenvectors relevant in the thermodynamic limit. We can find the probabilities of every brick configuration, or the configuration of the six spins in a hexagon in the original distorted kagomé lattice. This is related to the ^{51}V NMR study of Bert *et al.*,[19] because different local spin configurations will produce different magnetic fields on the V site. However, the authors of that experimental paper did not take into account the constraints on chirality variables; thus, their theoretical estimates of the probabilities of different local configurations are incorrect.

First we consider the brick configuration containing a collision of vertical domain walls. This corresponds to the local $\sqrt{3}\times\sqrt{3}$ configuration, which produces the largest magnetic field (three times of a single Cu if $\alpha\sim 1$; in general, the factor is $2+2\alpha^{-1}-\alpha^{-2}$) on the V site. However, since our eigenvectors do not contain collision, the probability of this local configuration is zero.

Next, we consider the configuration where there is one vertical domain wall and also one horizontal domain wall through the brick. This will produce a smaller magnetic field [$\sqrt{3}$ times of a single Cu if $\alpha\sim 1$; in general, the factor is $\sqrt{(5\alpha-2)/\alpha^3}$].

Notice that we have a particle-hole-like symmetry. For a subspace span (x) discussed in the previous paragraphs, where x contains vertical domain walls through some of the top-left edges of bricks, we can construct another subspace span $(\bar{x})$ from a "complementary" configuration $\bar{x}$, in which there is one vertical domain wall through a top-left edge of a brick if and only if there is no vertical domain wall through that edge in x.

Therefore, the probability that there is one vertical domain wall through the brick is one-half. The probability of a horizontal domain wall through the brick is clearly also one-half for the eigenvectors we consider. Combining these two factors, we have the probability of 25% for this type of local configuration. Note that whether the vertical domain wall is on the left- or right side will give another factor of one-half, hence, the 12.5% probabilities in Fig. 10 for the two configurations of this type.

Probability of other configurations can be derived in the similar fashion. However, all the other local configurations will produce very small magnetic field on the V site (for $\alpha\sim 1$). In particular, the configuration with no domain wall through the brick has a magnetic field $|2-2\alpha^{-1}|$ times a single Cu field, with the probability of 25%. The configuration with no vertical domain wall but a horizontal domain wall has the same magnetic field factor $|2-2\alpha^{-1}|$, with the probability of 25%. The two configurations with one vertical domain wall but no horizontal domain wall have the magnetic field factor $|\alpha-1|/\alpha^2$ and the total probability of 25% (12.5% each).

Based on these analyses, we argue that the 20% slow component observed in NMR[19] is not due to the local $\sqrt{3}\times\sqrt{3}$ configuration, but rather the configurations producing a smaller (factor of $\sqrt{3}$ rather than 3) magnetic field and with a theoretical probability of 25% (with one vertical and one horizontal domain wall).

APPENDIX B: DISPERSION OF QUADRATIC QUANTUM SPIN WAVE

In this appendix, we present the quadratic (or the so-called linear) quantum spin-wave dispersion of the distorted kagomé Heisenberg model. We notice that there is still a zero-energy band, and the spin-wave velocity of the dispersive branch vanishes in one direction in momentum space.

We start from Eq. (4) and do the Fourier transform of the bosonic fields,

$$b_{X,\mathbf{k}} = N^{-1/2}\sum_{\mathbf{R}} \exp[-i\mathbf{k}\cdot(\mathbf{R}+\mathbf{r}_X)]b_{X,\mathbf{R}},$$

where $X=A,B,C$ label the three sublattices and N is the number of unit cells. $\mathbf{R}$ are positions of unit cells, $\mathbf{r}_X$ are positions of the three basis sites within a unit cell, and $\mathbf{k}$ is the wave vector.

The quadratic Hamiltonian is then block diagonalized,

$$H_2 = \sum_{\mathbf{k}} \psi_{\mathbf{k}}^\dagger \cdot M(\mathbf{k}) \cdot \psi_{\mathbf{k}} + \text{constant},$$

where $\psi_{\mathbf{k}}^\dagger=(b_{A,\mathbf{k}}^\dagger, b_{B,\mathbf{k}}^\dagger, b_{C,\mathbf{k}}^\dagger, b_{A,-\mathbf{k}}, b_{B,-\mathbf{k}}, b_{C,-\mathbf{k}})$, $M(\mathbf{k})$ is a 6×6 Hermitian matrix, and the summation is over the $\mathbf{k}$ points in the BZ. Here, $M(\mathbf{k})$ can be written as

$$M(\mathbf{k}) = \begin{pmatrix} P & Q \\ Q & P \end{pmatrix}.$$

Here, P and Q are both 3×3 matrices as shown below, and we use the notation $c_1=\cos\left(\frac{k_1}{2}\right)$, $c_2=\cos\left(\frac{k_2}{2}\right)$, and $c_3=\cos\left(\frac{k_3}{2}\right)$, with $k_i=\mathbf{k}\cdot\mathbf{e}_i$ and $k_3=-k_1-k_2$,

$$P = \frac{1}{2\alpha}\begin{pmatrix} 4 & (2\alpha-1)c_3 & (2\alpha-1)c_2 \\ (2\alpha-1)c_3 & 4\alpha^2 & c_1 \\ (2\alpha-1)c_2 & c_1 & 4\alpha^2 \end{pmatrix},$$

$$Q = \frac{2\alpha+1}{2\alpha}\begin{pmatrix} 0 & c_3 & c_2 \\ c_3 & 0 & (2\alpha-1)c_1 \\ c_2 & (2\alpha-1)c_1 & 0 \end{pmatrix}.$$

We need to further diagonalize $M(\mathbf{k})$ by an SU(3,3) Bogoliubov transformation. Namely, we need an SU(3,3) matrix U such that

$$U^\dagger \tau U = \tau, \quad \tau = \begin{pmatrix} 1_{3\times 3} & 0 \\ 0 & -1_{3\times 3} \end{pmatrix},$$

and

$$U^\dagger M(\mathbf{k}) U = \begin{pmatrix} \omega(\mathbf{k}) & 0 \\ 0 & \omega(-\mathbf{k}) \end{pmatrix},$$

where $1_{3\times 3}$ is the 3×3 identity matrix, and $\omega(\mathbf{k})$ is a 3×3 diagonal matrix with three branches of spin dispersions as the diagonal elements, because of the inversion symmetry $\omega(\mathbf{k})=\omega(-\mathbf{k})$.

In isotropic kagomé model, P and Q commute and can be diagonalized simultaneously, which simplifies the calculation. However, for general α matrices, P and Q do not commute.

A simpler way to get the dispersion is to solve the eigenvalues of $\tau\cdot M(\mathbf{k})$. It is fairly simple to prove that the six eigenvalues of $\tau\cdot M(\mathbf{k})$ are $\pm\omega_i(\mathbf{k})$, $i=1,2,3$, indicating three branches.[16] The characteristic polynomial of $\tau\cdot M(\mathbf{k})$ is $x^6 - 2f_2x^4 + f_4x^2$. The dispersion is the following:

$$\omega_1 = 0, \quad \omega_{2,3} = \sqrt{f_2 \mp \sqrt{\Delta}},$$

where $\Delta = f_2^2 - f_4$ and

$$f_2 = 2\alpha^2 + 1 - 2\alpha^{-1} + 2\alpha^{-2} - (2\alpha^2 - 1)\cos(k_1) - \alpha^{-1}[\cos(k_2) + \cos(k_3)],$$

$$\Delta = 2\frac{(\alpha-1)^2}{\alpha^4}\{2 + \alpha^2 + \alpha^2\cos(k_1) - 2\alpha[\cos(k_2) + \cos(k_3)]\}.$$

Although the dispersion has become much more complicated than the kagomé case, the zero-energy band still exists.

When $\alpha=1$, $f_2^2 - f_4 = 0$, we have $\omega_2 = \omega_3 = \sqrt{3 - \cos(k_1) - \cos(k_2) - \cos(k_3)}$. For small $|\mathbf{k}|$, the dispersion becomes $\omega_2 = \omega_3 \sim \sqrt{k_1^2 + k_1k_2 + k_2^2} \propto |\mathbf{k}|$. Thus, we have two linear spin-wave branches.

However, as long as $\alpha \neq 1$, we have $\omega_2 \neq \omega_3$ and $\omega_3(\mathbf{k}=0) = 2|1-\alpha^{-1}| > 0$. We still have one Goldstone mode because $\omega_2(\mathbf{k}=0)=0$. However, the small wave vector dispersion is drastically changed, $\omega_2 \sim \sqrt{(\alpha^2 - 1/4)k_1^2} \propto |k_1|$. Namely, the spin-wave velocity in the k_2 direction (vertical direction in $\mathbf{k}$ space) vanishes.

APPENDIX C: CLASSICAL SPIN WAVE: QUADRATIC THEORY AND CHIRALITY INTERACTIONS

Let us start from Eq. (5), replace ϵ^y and ϵ^z by $\tilde{\epsilon}^y$ and $\tilde{\epsilon}^z$, and do the Fourier transforms of $\tilde{\epsilon}^y$ and $\tilde{\epsilon}^z$ (see the previous appendix for notation),

$$\tilde{\epsilon}^y_{X,\mathbf{k}} = N^{-1/2}\sum_{\mathbf{R}} \exp[-i\mathbf{k}\cdot(\mathbf{R}+\mathbf{r}_X)]\tilde{\epsilon}^y_{X,\mathbf{R}},$$

$$\tilde{\epsilon}^z_{X,\mathbf{k}} = N^{-1/2}\sum_{\mathbf{R}} \exp[-i\mathbf{k}\cdot(\mathbf{R}+\mathbf{r}_X)]\tilde{\epsilon}^z_{X,\mathbf{R}}.$$

The quadratic Hamiltonian can be block diagonalized,

$$\tilde{H}_2^y = \sum_{\mathbf{k}} \chi_{\mathbf{k}}^\dagger M_y(\mathbf{k})\chi_{\mathbf{k}},$$

$$\tilde{H}_2^z = \sum_{\mathbf{k}} \phi_{\mathbf{k}}^\dagger M_z(\mathbf{k})\phi_{\mathbf{k}},$$

where $\chi_{\mathbf{k}}^\dagger = (\tilde{\epsilon}^y_{A,-\mathbf{k}}, \tilde{\epsilon}^y_{B,-\mathbf{k}}, \tilde{\epsilon}^y_{C,-\mathbf{k}})$ and $\phi_{\mathbf{k}}^\dagger = (\tilde{\epsilon}^z_{A,-\mathbf{k}}, \tilde{\epsilon}^z_{B,-\mathbf{k}}, \tilde{\epsilon}^z_{C,-\mathbf{k}})$, and $M_{y,z}(\mathbf{k})$ are both 3×3 matrices, shown below, where we use the notation $c_1 = \cos\left(\frac{k_1}{2}\right)$, $c_2 = \cos\left(\frac{k_2}{2}\right)$, and $c_3 = \cos\left(\frac{k_3}{2}\right)$,

$$M_y(\mathbf{k}) = \alpha^{-1}\begin{pmatrix} 2 & -c_3 & -c_2 \\ -c_3 & 2\alpha^2 & (1-2\alpha^2)c_1 \\ -c_2 & (1-2\alpha^2)c_1 & 2\alpha^2 \end{pmatrix},$$

$$M_z(\mathbf{k}) = 2\begin{pmatrix} \alpha^{-1} & c_3 & c_2 \\ c_3 & \alpha & \alpha c_1 \\ c_2 & \alpha c_1 & \alpha \end{pmatrix}.$$

It is straightforward to check that $M_z(\mathbf{k})$ has a zero eigenvalue with (not normalized) eigenvector $(\alpha\sin(k_1/2), \sin(k_2/2), \sin(k_3/2))$ for all $\mathbf{k}$, and $M_y(\mathbf{k}=0)$ has a zero eigenvalue with eigenvector (1,1,1).

For small $|\mathbf{k}|$, the dispersion of the lowest branch of $M_y(\mathbf{k})$ is approximately $(1/6\alpha)(\alpha^2k_1^2 + k_1k_2 + k_2^2)$.

Now, we consider the calculation of the chirality interactions. Each chirality interaction is calculated by 36 terms in $(\tilde{H}_3)^2$; we show here an example in Fig. 2. Chiralities η_1 and η_5 are defined on triangles ABC and DEF in the distorted kagomé lattice, respectively. η_1 determines the sign of the angles between spins on ABC sites, $\theta_{AB} = \eta_1\theta_0$, $\theta_{BC} = -2\eta_1\theta_0$, and $\theta_{CA} = \eta_1\theta_0$. θ_{DF}, θ_{EF}, and θ_{FD} are determined

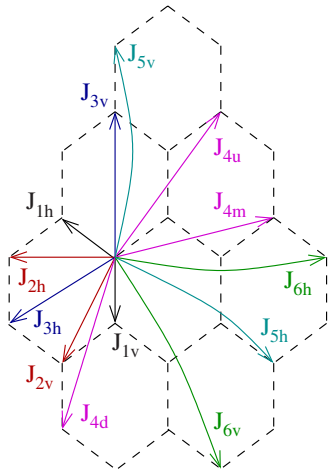

FIG. 11. (Color online) chirality-chirality couplings calculated here. Equivalent couplings under space group symmetry are not shown.

in the similar way by η_5, and $\theta_{ji}=-\theta_{ij}$. Plugging these into Eq. (5), then the relevant terms in $(\tilde{H}_3)^2$ are $2\eta_1\eta_5(h_{AB}+h_{BC}+h_{CA})(h_{DE}+h_{EF}+h_{FD})$, where

$$h_{AB}=\sin(\theta_0)(\tilde{\epsilon}_A^y\xi_B-\tilde{\epsilon}_B^y\xi_A),$$

$$h_{BC}=\sin(-2\theta_0)(\tilde{\epsilon}_B^y\xi_C-\tilde{\epsilon}_C^y\xi_B),$$

$$h_{CA}=\sin(\theta_0)(\tilde{\epsilon}_C^y\xi_A-\tilde{\epsilon}_A^y\xi_C).$$

Here, we use $\xi_i=[(\tilde{\epsilon}_i^y)^2+(\tilde{\epsilon}_i^z)^2]$ and $\theta_0=\arccos(-1/2\alpha)$, and h_{DE}, h_{EF}, h_{FD} are obtained by replacing subscripts ABC by DEF, respectively.

According to Eq. (6), the effective chirality-chirality coupling is $-T^2\langle(h_{AB}+h_{BC}+h_{CA})(h_{DE}+h_{EF}+h_{FD})\rangle_0$. Expanding this expression, we have 36 terms, each of the form $\langle\tilde{\epsilon}_i^y\xi_j\tilde{\epsilon}_k^y\xi_m\rangle_0$ which can be further expanded into four terms, $\langle\tilde{\epsilon}_i^y(\tilde{\epsilon}_j^y)^2\tilde{\epsilon}_k^y(\tilde{\epsilon}_m^y)^2\rangle_0+\langle\tilde{\epsilon}_i^y(\tilde{\epsilon}_j^y)^2\tilde{\epsilon}_k^y(\tilde{\epsilon}_m^z)^2\rangle_0+\langle\tilde{\epsilon}_i^y(\tilde{\epsilon}_j^z)^2\tilde{\epsilon}_k^y(\tilde{\epsilon}_m^y)^2\rangle_0+\langle\tilde{\epsilon}_i^y(\tilde{\epsilon}_j^z)^2\tilde{\epsilon}_k^y(\tilde{\epsilon}_m^z)^2\rangle_0$. Each term in the last expression can be expanded into a sum of products of three two-point correlators by Wick's theorem. The two-point correlators are computed following the standard routine in all quadratic theory, e.g.,

$$\langle\tilde{\epsilon}_{A,0}^y\tilde{\epsilon}_{B,\mathbf{R}}^y\rangle_0=\int d^2\mathbf{k}[M_y^{-1}(\mathbf{k})]_{AB}e^{i\mathbf{k}\cdot(\mathbf{R}+\mathbf{r}_B-\mathbf{r}_A)}$$

for the A-sublattice site in the unit cell at origin and the B-sublattice site in the unit cell at position $\mathbf{R}$. We calculated up to the sixth neighbor chirality couplings (Fig. 11). Some data are presented in Table II.

All the above mentioned calculations in Appendix B and in this appendix were done in the software MATHEMATICA.

[1] Z. Hiroi, M. Hanawa, N. Kobayashi, M. Nohara, H. Takagi, Y. Kato, and M. Takigawa, J. Phys. Soc. Jpn. **70**, 3377 (2001).
[2] M. P. Shores, E. A. Nytko, B. M. Bartlett, and D. G. Nocera, J. Am. Chem. Soc. **127**, 13462 (2005).
[3] Oleg Tchernyshyov, R. Moessner, and S. L. Sondhi, Phys. Rev. Lett. **88**, 067203 (2002).
[4] R. Ramesh and N. Spaldin, Nat. Mater. **6**, 21 (2007).
[5] Sang-Wook Cheong and Maxim Mostovoy, Nat. Mater. **6**, 13 (2007).
[6] M. A. Lafontaine, A. L. Bail, and G. Ferey, J. Solid State Chem. **85**, 220 (1990).
[7] R. Youngblood, J. D. Axe, and B. M. McCoy, Phys. Rev. B **21**, 5212 (1980).
[8] M. J. Harris, S. T. Bramwell, D. F. McMorrow, T. Zeiske, and K. W. Godfrey, Phys. Rev. Lett. **79**, 2554 (1997).
[9] L. Balents, M. P. A. Fisher, and S. M. Girvin, Phys. Rev. B **65**, 224412 (2002); S. V. Isakov, Y. B. Kim, and A. Paramekanti, Phys. Rev. Lett. **97**, 207204 (2006).
[10] M. Hermele, M. P. A. Fisher, and L. Balents, Phys. Rev. B **69**, 064404 (2004); A. Banerjee, S. V. Isakov, K. Damle, and Y. B. Kim, arXiv:cond-mat/0702029 (unpublished).
[11] A. Paramekanti, L. Balents, and M. P. A. Fisher, Phys. Rev. B **66**, 054526 (2002).
[12] C. L. Henley and E. P. Chan, J. Magn. Magn. Mater. **140**, 1693 (1996).
[13] A. Chubukov, Phys. Rev. Lett. **69**, 832 (1992).
[14] P. Chandra, P. Coleman, and I. Ritchey, J. Phys. I **3**, 591 (1993).
[15] D. A. Huse and A. D. Rutenberg, Phys. Rev. B **45**, 7536 (1992).
[16] S. Sachdev, Phys. Rev. B **45**, 12377 (1992).
[17] R. Moessner and J. T. Chalker, Phys. Rev. B **58**, 12049 (1998).
[18] R. J. Baxter, J. Math. Phys. **11**, 784 (1970).
[19] F. Bert, D. Bono, P. Mendels, F. Ladieu, F. Duc, J.-C. Trombe, and P. Millet, Phys. Rev. Lett. **95**, 087203 (2005).
[20] An experimental caveat here is that no analogous signal is seen in μSR at the same temperatures (Ref. 36), perhaps due to different local environments of the two probes.
[21] J. S. Helton, K. Matan, M. P. Shores, E. A. Nytko, B. M. Bartlett, Y. Yoshida, Y. Takano, A. Suslov, Y. Qiu, J.-H. Chung, D. G. Nocera, and Y. S. Lee, Phys. Rev. Lett. **98**, 107204 (2007).
[22] Oren Ofer, Amit Keren, Emily A. Nytko, Matthew P. Shores, Bart M. Bartlett, Daniel G. Nocera, Chris Baines, and Alex Amato, arXiv:cond-mat/0610540 (unpublished).
[23] P. Mendels, F. Bert, M. A. de Vries, A. Olariu, A. Harrison, F. Duc, J. C. Trombe, J. Lord, A. Amato, and C. Baines, Phys. Rev. Lett. **98**, 077204 (2007).
[24] T. Imai, E. A. Nytko, B. M. Bartlett, M. P. Shores, and D. G. Nocera, arXiv:cond-mat/0703141 (unpublished).
[25] J. Villain, J. Phys. (Paris) **41**, 1263 (1980); C. L. Henley, Phys. Rev. Lett. **62**, 2056 (1989).
[26] J. N. Reimers and A. J. Berlinsky, Phys. Rev. B **48**, 9539 (1993).
[27] E. Brezin and J. Zinn-Justin, Phys. Rev. Lett. **36**, 691 (1976), Phys. Rev. B **14**, 3110 (1976).
[28] J. T. Chalker, P. C. W. Holdsworth, and E. F. Shender, Phys. Rev. Lett. **68**, 855 (1992).
[29] D. Bergman, J. Alicea, E. Gull, S. Trebst, and L. Balents, Nat. Phys. **3**, 487 (2007).
[30] A. B. Harris, C. Kallin, and A. J. Berlinsky, Phys. Rev. B **45**, 2899 (1992).
[31] ALPS collaboration, F. Alet *et al.*, J. Phys. Soc. Jpn. **74**, 30 (2005).
[32] N. Elstner and A. P. Young, Phys. Rev. B **50**, 6871 (1994).
[33] W. Apel, T. Yavors'kii, and H.-U. Everts, J. Phys.: Condens. Matter **19**, 145255 (2007).
[34] Y. Ran, M. Hermele, P. A. Lee, and X.-G. Wen, Phys. Rev. Lett. **98**, 117205 (2007).
[35] S. Ryu, O. I. Motrunich, J. Alicea, Matthew, and P. A. Fisher, Phys. Rev. B **75**, 184406 (2007).
[36] A. Fukaya, Y. Fudamoto, I. M. Gat, T. Ito, M. I. Larkin, A. T. Savici, Y. J. Uemura, P. P. Kyriakou, G. M. Luke, M. T. Rovers, K. M. Kojima, A. Keren, M. Hanawa, and Z. Hiroi, Phys. Rev. Lett. **91**, 207603 (2003).
[37] T. Yavors'kii, W. Apel, and H.-U. Everts, arXiv:0704.1441 (unpublished).